Nanoscale

View Online
Dynamic Article Links

Cite this: *Nanoscale*, 2011, **3**, 2709

www.rsc.org/nanoscale

PAPER

Substrate effects on the electron-beam-induced deposition of platinum from a liquid precursor

Eugenii U. Donev, Gregory Schardein, John C. Wright and J. Todd Hastings*

Received 10th January 2011, Accepted 2nd February 2011
DOI: 10.1039/c1nr10026b

Focused electron-beam-induced deposition using bulk liquid precursors (LP-EBID) is a new nanofabrication technique developed in the last two years as an alternative to conventional EBID, which utilizes cumbersome gaseous precursors. Furthermore, LP-EBID using dilute aqueous precursors has been demonstrated to yield platinum (Pt) nanostructures with as-deposited metal content that is substantially higher than the purity achieved by EBID with currently available gaseous precursors. This advantage of LP-EBID—along with the ease of use, low cost, and relative innocuousness of the liquid precursors—holds promise for its practical applicability in areas such as rapid device prototyping and lithographic mask repair. One of the feasibility benchmarks for the LP-EBID method is the ability to deposit high-fidelity nanostructures on various substrate materials. In this study, we report the first observations of performing LP-EBID on bare and metal-coated silicon–nitride membranes, and compare the resulting Pt deposits to those obtained by LP-EBID on polyimide membranes in terms of nucleation, morphology, size dependence on electron dose, and purity.

Introduction

Two of the earliest uses of electron beams to *intentionally* deposit materials were reported by Christy[1] in 1960 and Baker and Morris[2] in 1961, but until the 1990s electron-induced processing with focused beams remained only sporadically explored. In recent years, the rapid progress of nanoscience and nanotechnology has generated vigorous activity in this field, and no fewer than six review articles[3–8] and one book[9] about nanoscale e-beam-induced processing have been published since 2006.

Focused e-beam-induced deposition (EBID) has traditionally relied on the electron-stimulated dissociation and desorption of adsorbed or condensed *gaseous* precursors, many of which are cumbersome to use in terms of toxicity, instability or cost. Most gas-phase EBID processes also suffer from a chronic low purity of the deposits, especially severe for the prevalent type of gaseous precursors, metal–organics, which typically produce deposits with carbon concentrations several times higher than those of the desired metals.[8,10]

This paper reports on recent new developments in focused e-beam-induced deposition from *bulk liquid* precursors, LP-EBID, as an alternative to gas-phase EBID. LP-EBID was first demonstrated[11] in 2009 and is currently being pursued as a viable nanofabrication technique.[12–14] Here we compare deposition of platinum (Pt) nanostructures by LP-EBID on three different materials: polyimide, silicon nitride, and gold. We observe marked differences in deposit morphology and size, and in the electron dose necessary to initiate deposition on each substrate material. On the other hand, we show that the purity of our Pt deposits is consistently high regardless of substrate and remains one of the main advantages of the LP-EBID process over its gas-phase counterpart.

Department of Electrical and Computer Engineering, and Center for Nanoscale Science and Engineering (CeNSE), University of Kentucky, Lexington, KY, 40506, USA. E-mail: hastings@engr.uky.edu

Experimental details

Precursor, capsules, substrates

All Pt nanostructures described in this work were fabricated by LP-EBID from dilute aqueous solutions of chloroplatinic acid (1 wt% H_2PtCl_6 from Sigma-Aldrich in deionized water) in a standard electron-beam lithography (EBL) system (Raith e_LiNE). Two types of sealed capsules were used to house the liquid precursor inside the e-beam chamber and separate it from the vacuum: (i) an all-commercial product (QuantomiX QX-102 WETSEM), which holds up to 0.015 mL of liquid *via* a polyimide membrane supported on a metal grid[15] (Fig. 1(a)); (ii) a home-built sample holder, designed to incorporate a silicon window frame with a low-stress silicon–nitride membrane[16] ($Si_{x>3}N_4$, from SPI Supplies), with a liquid capacity of about 0.001 mL (Fig. 1(b)). Both the polyimide and Si_xN_4 membranes have a nominal thickness of 150 nm; Si_xN_4 membranes were used either as supplied by the manufacturer or with a 6 nm thick bilayer of chromium (Cr: 3 nm on top of Si_xN_4, for better adhesion) and gold (Au: 3 nm on top of Cr), coated by e-beam evaporation on the liquid-side surface of the Si_xN_4 membrane (Fig. 1(c)). Thus, we were able to compare LP-EBID of Pt

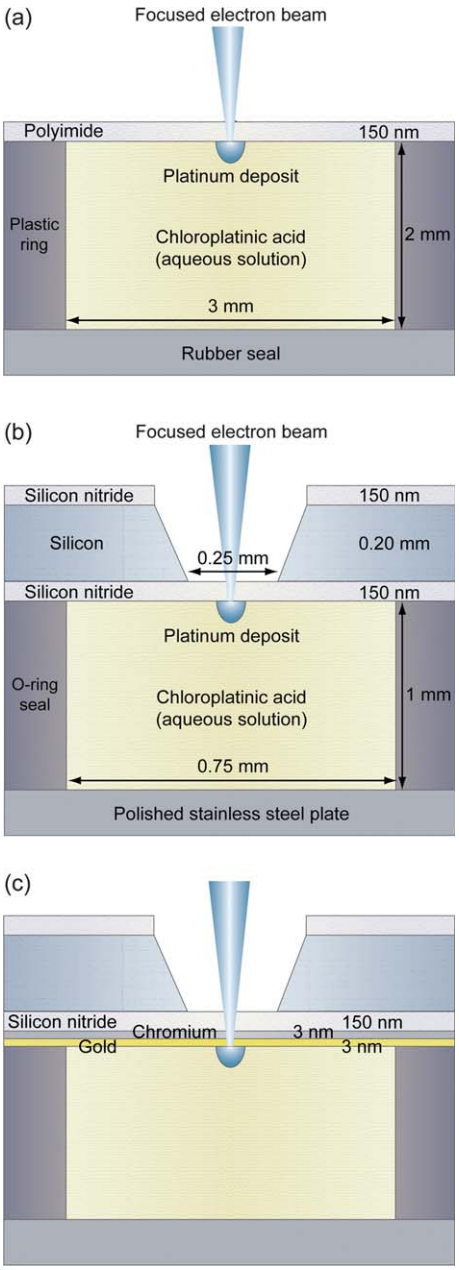

Fig. 1 Schematics of the experimental capsules used in this work, showing different substrate materials: (a) polyimide (the supporting metal grid on the vacuum side is not shown); (b) bare (*i.e.*, uncoated) Si_xN_4; (c) Au + Cr-coated Si_xN_4 (the omitted parameters are the same as in part (b)).

nanostructures on three different substrate materials: polyimide, bare Si_xN_4, and Au + Cr-coated Si_xN_4.

LP-EBID parameters

As sketched in Fig. 1, LP-EBID occurs when the primary electron beam enters the sealed capsule through a thin membrane (substrate), interacts with the membrane and the aqueous solution containing ion complexes of the desired metal (here: $[PtCl_6]^{2-}$) *via* a cascade of scattering events and stimulated chemical reactions, and deposits the reduced metal species ($Pt^{4+} \rightarrow Pt^0$) at the membrane–liquid interface. We used a primary e-beam energy of 20 keV for all depositions, but varied the beam current depending on the substrate material: ~0.2 nA for polyimide and 1.3 nA for bare/coated Si_xN_4. Different beam currents were chosen because the minimum doses necessary to observe Pt deposition on bare and coated Si_xN_4 membranes were about 10^2 to 10^3 times larger than the threshold dose for the polyimide membranes.

The primary electron beam was focused either on colloidal Au nanoparticles drop-cast on the vacuum-side surface of the membrane, or on small initial deposits of Pt at the membrane–liquid interface. By means of the Raith pattern generator, the nanoscale beam impinged at each predetermined dot location for a given dwell time (hence, electron dose)—the longer the dwell, the larger the resulting deposit. Similar to gas-phase EBID, and unlike resist-based EBL, LP-EBID is a direct-write nanofabrication technique, since deposition generally proceeds without chemical or physical post-processing of the patterned areas other than rinsing in deionized water and blow-drying with filtered nitrogen.

Characterization of Pt deposits

After the LP-EBID process, the deposits were imaged by scanning electron microscopy (SEM: Raith e_LiNE). We show two types of SEM images here: (i) planar overviews of entire arrays of Pt nanoparticles (NPs), taken *in situ* through the membrane (*i.e.*, immediately after LP-EBID, liquid in place, deposits facing down); and (ii) tilted-view images of NPs, taken *ex situ* (*i.e.*, no liquid, deposits facing "up") at an angle of 45° or 70° between the incident beam and the normal to the membrane surface. For all tilt-view micrographs, the corresponding scale bars apply only horizontally across the page (*i.e.*, along the axis of rotation of the tilt) and the near-to-far depth perspective runs bottom to top in each image.

The purity of the deposits was quantified by means of energy-dispersive X-ray spectroscopy (EDS: Hitachi S-3200 SEM at 20 keV, equipped with Evex lithium-drifted silicon detector), in conjunction with Monte Carlo simulations using public-domain software for X-ray microanalysis from NIST[17–19] and incorporating the physical parameters of our EDS detector. The simulations, which model the elastic and inelastic scattering and characteristic X-ray generation of energetic electrons incident upon the sample and substrate materials, allowed us to place upper bounds on the amount of chlorine (Cl) contamination in our Pt deposits, typically 15–20 at% (see below and ref. 11).

Results and discussion

Electron-beam-induced deposition at solid–liquid interfaces is a relatively new nanofabrication method, hence the detailed nature, sequence, and dominance of the underlying physicochemical processes remain scarcely studied,[13,20] although *in situ* electron microscopy has been used to study in detail the real-time kinetics of electrochemical nucleation and growth of copper in liquid.[21,22] In addition to dissolved precursor ions and injected primary electrons, the interaction volume of the focused beam contains a dynamical mixture of various species: backscattered,

secondary, and solvated electrons; ions and radicals; interfacial electric double layers; surface charges; and electron–hole pairs. How each species contributes to the overall LP-EBID mechanism is currently unknown. Broadly speaking, metallic deposits form as a result of electron-impact molecular dissociation of the metal–ion complexes in solution, chemical reduction of the freed metal cations, nucleation at favorable interfacial sites (and possibly in the bulk of the liquid), and subsequent growth of the initial nuclei under continued e-beam irradiation.

Effects of the substrate on the nucleation and growth of deposits have been noted in previous EBID studies,[4,13,20,23–27] which seem to suggest that the accumulation of charges at substrate surfaces and/or sharp features somehow influences the deposition mechanism. However, as Hagen *et al.*[26] and Song and Furuya[4] point out, clear understanding of the role of the substrate in EBID is still lacking and key questions remain unanswered.

Growth and morphology of Pt deposits

The following three subsections and accompanying SEM images present our latest findings regarding the nucleation and growth of Pt nanostructures deposited by LP-EBID on different substrate materials.

Polyimide substrate. We have previously reported on LP-EBID of Pt and Au nanostructures on this substrate material.[11,12,14] Specifically for Pt NPs on QuantomiX membranes (Fig. 1(a)) deposited at moderate e-beam doses (<200 pC per NP), we usually obtain deposits like those shown in Fig. 2. In the 'dose array' of 11 × 11 Pt NPs in Fig. 2(a), each NP along a vertical column was deposited with the same nominal dose, while the dose per NP increased by 10 pC from left to right along the horizontal rows: 10 pC per NP (leftmost column, enclosed by dashed line) to 110 pC per NP (rightmost column). The enclosed column of NPs in Fig. 2(a) provides an estimate of the threshold dose for LP-EBID of Pt on the polyimide substrate: 10 pC per NP. This value is in good agreement with our previous findings in ref. 12, where the SEM images did not show any Pt deposits for doses lower than 5 pC per NP. It is unclear at this point whether 5 pC (3×10^7 primary electrons) is a minimum dose required for creating a preferential nucleation site on the substrate or for dissociating enough precursor molecules to form a stable nucleus, or both.

Tilt-view *ex situ* micrographs of the dose array in Fig. 2(a) are shown in parts (b) and (c). It is evident from these images that the Pt NPs (i) grew out of e-beam-induced indentations in the membrane, (ii) have mostly pillar-like shapes, and that (iii) the high-dose end of the pattern became distorted after the deposition (*cf.* Fig. 2(a)), probably during the drying step. Drying with supercritical carbon dioxide can be utilized instead to better preserve pattern fidelity, since it is a method that removes aqueous solvents from surfaces while eliminating the capillary forces present during normal drying.[28] The indentation features were already observed by atomic force microscopy (AFM) in the first report[11] on LP-EBID, but the tilt-view SEM images

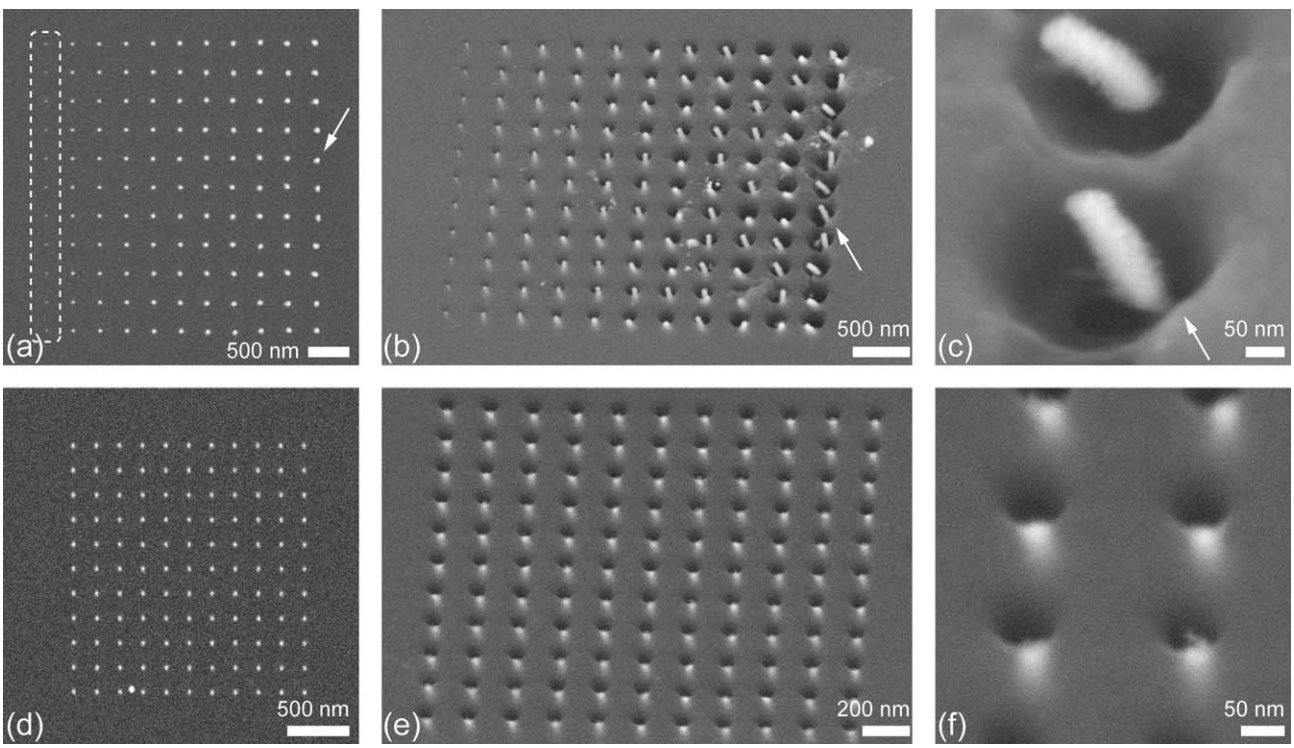

Fig. 2 SEM images of Pt deposits on polyimide; slanted arrows point to the same NP. (a) *In situ* planar-view of dose array of 11 × 11 NPs (350 nm pitch), with doses constant along each vertical column and increasing left to right along each horizontal row: 10–110 pC per NP by 10 pC per column; dashed line encloses NPs deposited at threshold dose of 10 pC per NP. (b and c) *Ex situ* tilted views (45°) of the dose array in part (a) at different magnifications. (d) *In situ* planar-view of 11 × 11 NP array (200 nm pitch) deposited at 14 pC per NP; the brighter dot at bottom left is one of the colloidal gold NPs used for focusing. (e and f) *Ex situ* tilted views (45°) of the array in part (d) at different magnifications.

presented here provide a better visualization of their morphology in relation to the embedded deposits and also reveal that the lateral size of an indentation increases with increasing e-beam dose, regardless of the lateral size of the NP it harbors.

Parts (d), (e) and (f) of Fig. 2 show another typical outcome of Pt deposition on the polyimide membrane. In this NP array, each dot received a nominal dose of 14 pC and there is little variation in the intensity of the imaging signal among the particles. Image analysis determined the average lateral diameter to be 45 ± 2 nm, in agreement with the previously reported dependence of NP size on e-beam dose in ref. 12. The tilted views of the array (Fig. 2(e) and (f)) again display membrane indentations with embedded deposits, some of which protrude out of the holes, but just barely.

Occasionally, however, deposition on the polyimide membrane would proceed at a much higher rate and with much more pronounced proximity effects, as was the case for some of the Pt depositions we described in ref. 11 as well as for those shown here in Fig. 3. (This type of 'proximity effect', caused by the spraying of secondary and/or forward-scattered electrons from the currently fabricated structure, occurs when structures fabricated at earlier times in the deposition sequence continue to grow, even though the impingement spot of the primary electron beam has already moved some distance away.)[7] The two arrays of Pt NPs are shown in full in lower-magnification, planar-view, *in situ* (Fig. 3(a)) and higher-magnification, tilt-view, *ex situ* (Fig. 3(b)) SEM images. The arrays received the same nominal dose, 14 pC per NP, as the array in Fig. 2(b), yet the resulting deposits clearly differ. We believe the monotonic non-uniformities of the deposits in Fig. 3 are due to the above-mentioned proximity effect, since they developed commensurately with the starting positions (denoted by dashed circles in (a)) and directions (dashed arrows in (a)) of the e-beam deposition scans, *i.e.*: earlier (in time) NPs have grown to much larger sizes than later NPs because of continual accrual of material during the entire deposition sequence. At even higher magnifications, tilt-view images of the deposits (upper array: Fig. 3(c); lower array: Fig. 3(d) and (e)) reveal two types of features: (i) bright mushroom-shaped Pt particles, complete with caps and stems, and (ii) somewhat less bright stems underneath even darker crescents at the locations of the smallest deposits. The latter type of feature we attribute again to indentations into the polyimide membrane, filled with kernels of Pt material. In fact, AFM characterization of the lower array in Fig. 3(a) confirmed the presence of indentations for the bottom two horizontal rows of the array (see Fig. 2 in ref. 11). The precise depth of the indentations into the polyimide membrane is unknown, though it is presumably less than the membrane thickness (150 nm)—otherwise, some of the liquid precursor would have leaked out of the capsule and into the vacuum chamber, causing a change in the pressure reading, which was not the case. On the other hand, the indentations could well run through the entire membrane thickness without precursor leakage if the Pt deposits formed quickly enough to plug the holes. Obtaining a cross-sectional view of the deposits and the membrane, for example by focused ion-beam milling, would help resolve this ambiguity. In any case, we speculate that the formation of indentations in the polyimide substrate (i) facilitates the nucleation step of the LP-EBID process and (ii) helps to constrain the lateral growth of the deposited features at lower electron doses, at least until the deposits have grown large enough to protrude out of the indentations, subsequently either "blooming" outwards into mushroom-cap shapes (Fig. 3) or continuing to grow into pillars of at least 5 : 2 aspect ratios (Fig. 2(c)). At present, we do not know what factors steer the deposition process into one or the other of these growth modes.

Bare silicon–nitride substrate. LP-EBID of Pt on uncoated Si_xN_4 membranes proceeded rather differently compared to deposition on polyimide membranes, though there was also a similarity (see below). Fig. 4(a) shows an *in situ*, planar-view image of a dose array of nominally 11×11 Pt NPs, in which only six of the columns are visible as the lowest five doses failed to produce visible deposits. The threshold dose for deposition (enclosed by a dashed line in Fig. 4(a)) was 3.0 nC per NP,

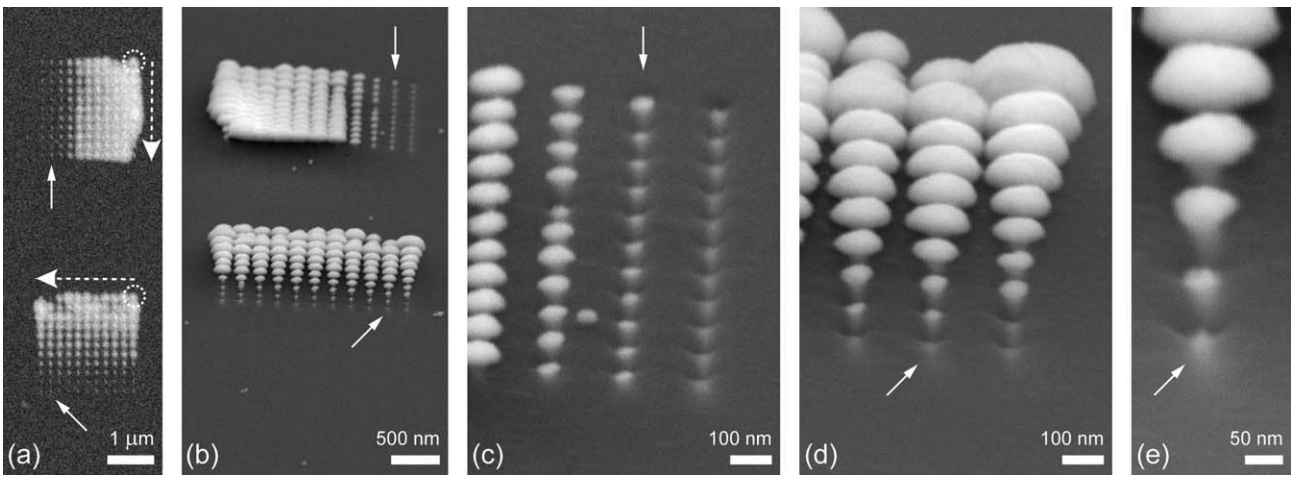

Fig. 3 SEM images of Pt deposits on polyimide; small slanted and vertical arrows point, respectively, to the same NPs across images. (a) *In situ* planar-view of two 11×11 NP arrays (200 nm pitch) deposited at 14 pC per NP; dashed circles and large dashed arrows indicate, respectively, origin and direction of the e-beam scans during deposition. (b) *Ex situ* tilted view (70°) of both arrays. (c) *Ex situ*, tilted, higher-magnification view of part of the upper array. (d and e) *Ex situ*, tilted (70°), higher-magnification views of parts of the lower array.

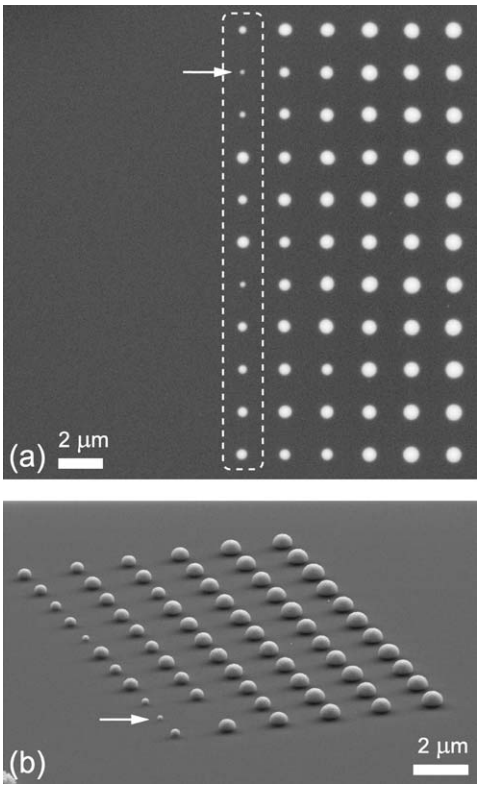

Fig. 4 SEM images of Pt deposits on bare Si_xN_4; horizontal arrows point to the same NP. (a) *In situ* planar-view of dose array of 11 × 11 NPs (2000 nm pitch), with doses constant along each vertical column and increasing left to right along each horizontal row: 0.5–5.5 nC per NP by 0.5 nC per column; dashed line encloses NPs deposited at threshold dose of 3.0 pC per NP. (b) *Ex situ* tilted view (70°) of the dose array, with one NP missing (probably detached during post-deposition rinsing).

300 times larger than the threshold dose on polyimide (see previous subsection), so we used a higher beam current (1.3 nA) to speed up deposition on the Si_xN_4 substrates, at the expense of reduced resolution and larger overall sizes of the deposited Pt NPs. Fig. 5 illustrates this trade-off: both patterns received nominally equal doses, 10 nC per NP, but the pattern in Fig. 5(a) was written at a beam current of 0.15 nA, took 15 min to deposit and yielded NPs with an average lateral diameter of 335 ± 15 nm, whereas the identical pattern in Fig. 5(b) took 2 min at 1.3 nA and gave 1010 ± 55 nm NPs. Note also the large variations in diameter among the threshold-dose NPs in Fig. 4(a)—from 270 to 680 nm—and that even the smallest NP in Fig. 4(a) (marked by arrow) significantly exceeds in lateral size any of the NPs on polyimide in Fig. 2.

Furthermore, *ex situ*, tilt-view images (Fig. 4(b) and 6) suggest that all but the smallest Pt deposits assume a near-hemispherical (mushroom-cap) shape on bare Si_xN_4. At first glance these large NPs look quite similar to the "bloomed-out" NPs on polyimide (Fig. 3(d) and (e)), but there is also an important difference in that the former NPs have no stems rooting them to the Si_xN_4 membrane. In other words, the electron–substrate–precursor interactions do not create indentations in the ceramic material as they do in the polyimide (Fig. 2 and 3). Judging by the large contact angles between particles and substrate, the Pt deposits exhibit poor wettability on Si_xN_4, which is especially evident in Fig. 6(b) where the NPs are nearly spherical and seemingly "float" on the substrate, and in Fig. 7 where one of the NPs (marked by arrow) sits partially raised above the substrate. Weak adhesion to the membrane is probably why a particle is missing from the *ex situ* image of the dose array (Fig. 4(b), second column/row from left/bottom), whereas it was clearly present in the *in situ* image (Fig. 4(a)) taken immediately after deposition.

Regarding nucleation of the Pt deposits on bare Si_xN_4, we hypothesize the following. At moderate doses, the electron beam cannot sufficiently alter the otherwise smooth surface of the ceramic membrane, which remains mostly devoid of potent nucleation sites. Thus, accrual of enough Pt atoms to form stable nuclei is hindered, until a certain (likely location-dependent) cumulative amount of charge—much larger than the threshold dose in the polyimide case—has been delivered to the impingement area of the substrate. In the absence of discernible indentations in the Si_xN_4, the nature of the e-beam-induced surface modifications that become favorable nucleation sites is unknown, with charging being a potential mechanism.[24,25]

Once a stable deposit begins forming, growth continues with relative ease, since the already accumulated material serves as

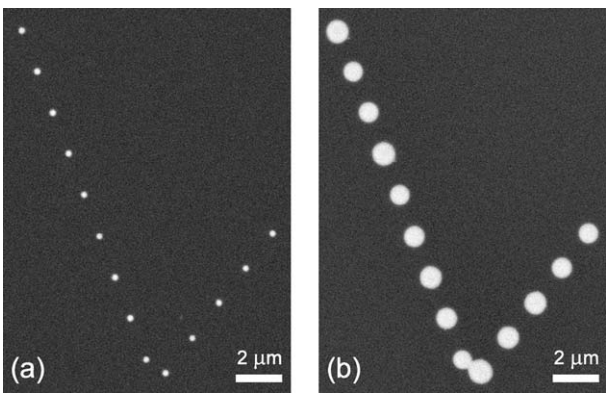

Fig. 5 *In situ* planar-view SEM images of Pt NPs on bare Si_xN_4 deposited at 10 nC per NP but at different e-beam currents: (a) 0.15 nA and (b) 1.3 nA.

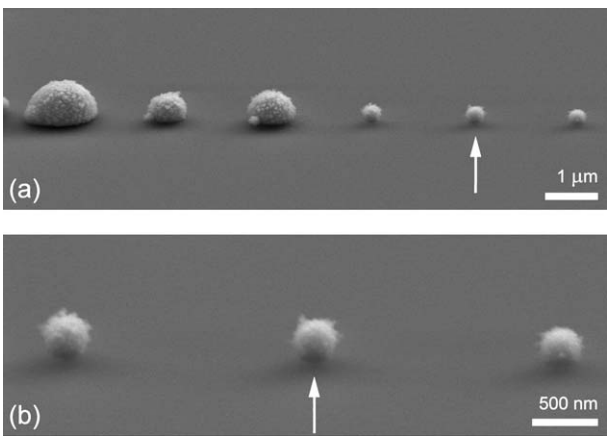

Fig. 6 *Ex situ* tilt-view (70°) SEM images of Pt deposits on bare Si_xN_4; vertical arrows point to the same NP. (a) Lower and (b) higher magnifications.

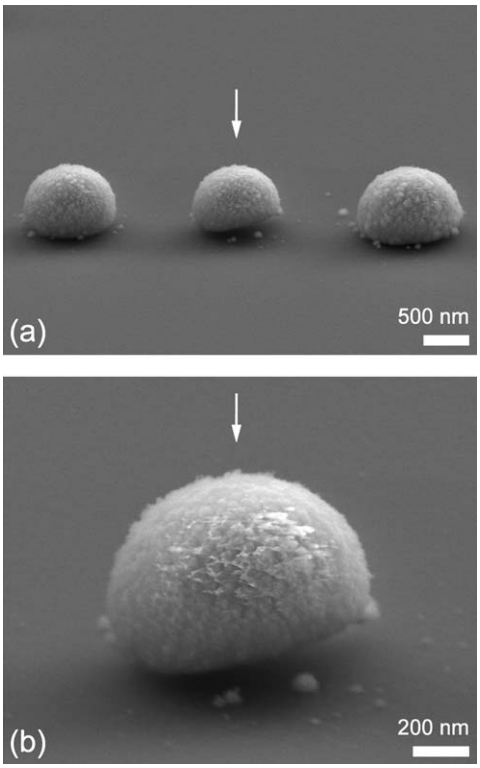

Fig. 7 *Ex situ* tilt-view (70°) SEM images of Pt deposits on bare Si_xN_4; vertical arrows point to the same NP. (a) Lower and (b) higher magnifications.

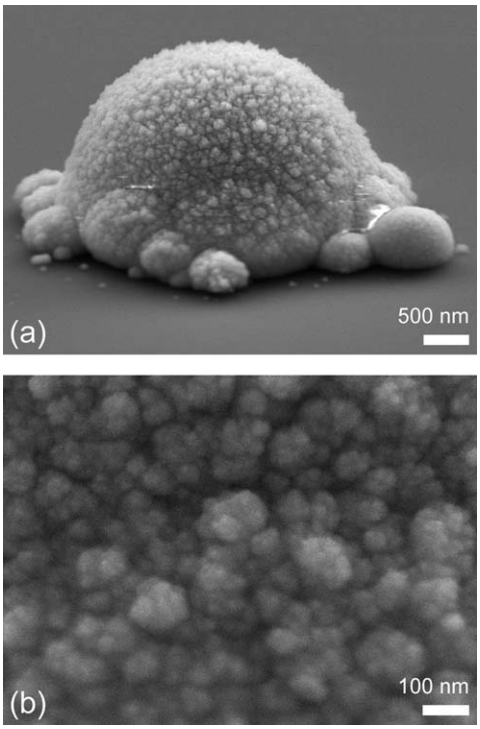

Fig. 8 *Ex situ* tilt-view (70°) SEM images of Pt deposit on bare Si_xN_4. (a) Lower and (b) higher magnifications.

a base to which newly dissociated metal ions/atoms can preferentially attach. In fact, prolonged *in situ* imaging of the deposits results in their continued growth, as demonstrated in Fig. 6(a). There, all six NPs were initially deposited at the same dose, but the three larger NPs on the left were then imaged for about three minutes *in situ*, in continuous-scan mode and at high-enough magnifications as to avoid directly imaging the rightmost three NPs; thus, the latter deposits remained relatively small and spherical. Another example of the continual accrual of material under prolonged *in situ* imaging is shown in Fig. 8. The large structure in Fig. 8(a) started out as a 400 nm NP and grew to 4000 nm after extensive scanning *in situ*; a magnified view of the particle's surface reveals texture with grain sizes of 50 nm and smaller (Fig. 8(b)).

Coated silicon–nitride substrate. In order to further investigate the role of the substrate surface, we deposited Pt NPs on Si_xN_4 coated with a 6 nm thick Au + Cr bilayer (3 nm Au layer being in contact with the liquid precursor). The reason for coating the substrate was that the relatively rough surface of the Au film might provide an inherently higher density of potent sites for nucleating the LP-EBID process than would the smooth surface of the uncoated Si_xN_4 membrane. Moreover, the Au was expected to enhance the wetting and adhesion of the Pt to the membrane. However, the results (Fig. 9) were not straightforward to interpret.

Fig. 9(a) is a planar-view, *in situ* micrograph of a dose array of 11 × 11 Pt NPs on Au + Cr-coated Si_xN_4 with a threshold dose of 4 nC per NP (enclosed by dashed line), comparable to the threshold dose for bare Si_xN_4 (3 nC per NP). For the 11 × 3 dose array in Fig. 9(b), the threshold dose was even higher, 15 nC per NP (enclosed by dashed line), presumably because the larger spacing between the NPs resulted in less parasitic deposition due to the proximity effect discussed earlier. In any case, the Au film apparently does not promote easier nucleation of the Pt deposits on Si_xN_4, since the threshold dose for LP-EBID actually increased for the coated membrane. On the other hand, the coated substrate allows for the deposition of higher-resolution patterns, such as the 200 nm pitch NP array shown in the inset of Fig. 9(b), unlike the bare Si_xN_4 substrate whereon attempts to deposit dense NP arrays resulted in smeared blocks of Pt (not shown).

Tilted *ex situ* views of the NPs in Fig. 9(a) and (b) are presented in parts (c and e) and (d and f), respectively. Visual comparison of the micrographs points to largely different morphologies for NPs deposited at different doses, namely: (i) lower-dose deposits resemble sections of spheres embedded in crater-like indentations in the Au (or Au + Cr) film(s), while (ii) higher-dose deposits (above ~25 nC per NP) look like pillars protruding out of holes in the surface and growing vertically rather than horizontally—unlike the hemispherical NPs (mushroom caps) on bare Si_xN_4 discussed earlier. Thus, in addition to inhibiting nucleation, the Au surface seems to constrain the lateral growth of the Pt deposits. For instance, the average lateral diameter of the largest NPs in Fig. 9(b) is 285 ± 10 nm at a dose of 55 nC per NP, whereas the largest NPs on bare Si_xN_4 in Fig. 4(a) are 880 ± 25 nm at a dose of only 5.5 nC per NP. A possible explanation for the different roles of bare and coated Si_xN_4 substrates in LP-EBID of Pt involves the accumulation and dissipation of charge. If substrate charging does indeed

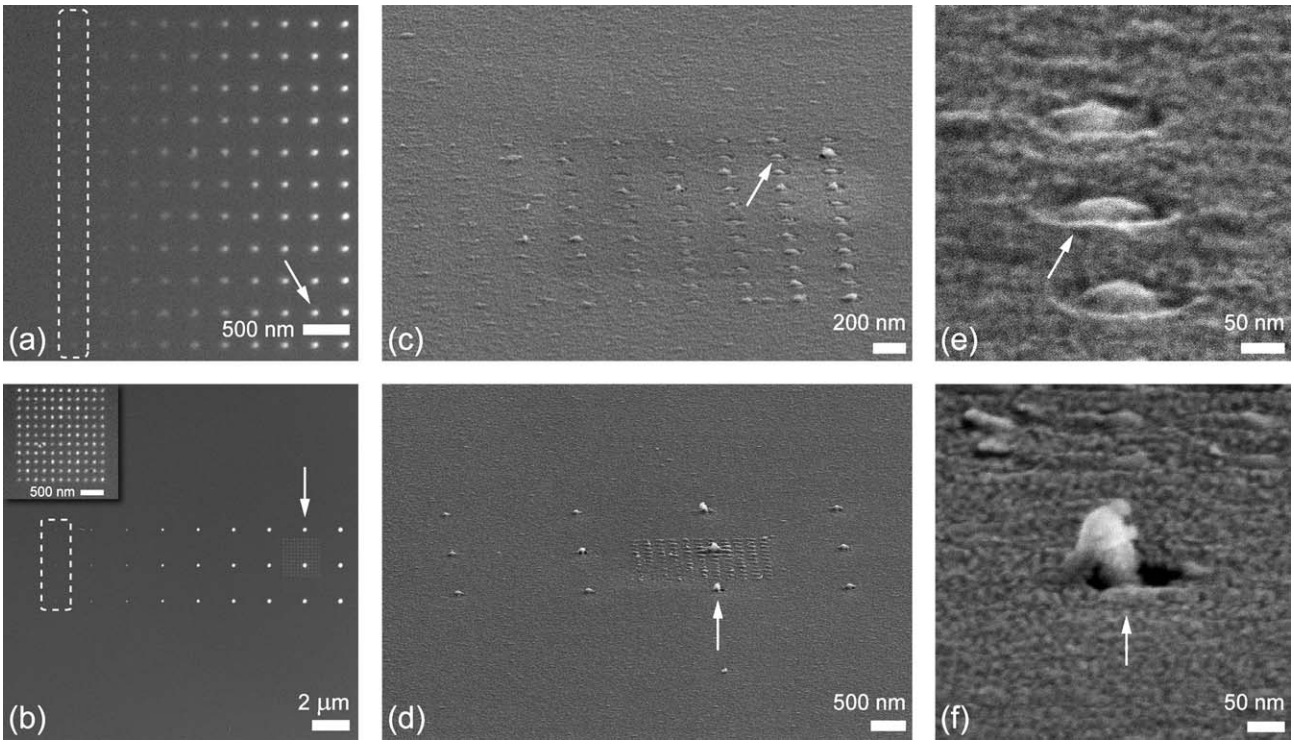

Fig. 9 SEM images of Pt deposits on Au + Cr-coated Si_xN_4; slanted and vertical arrows point, respectively, to the same NPs across images. (a) *In situ* planar-view of dose array of 11 × 11 NPs (350 nm pitch), with doses constant along each vertical column and increasing left to right along each horizontal row: 2–22 nC per NP by 2 nC per column; dashed line encloses NPs deposited at threshold dose of 4 pC per NP. (b) *In situ* planar-view of dose array of 11 × 3 NPs (2000 nm pitch), with doses constant along each vertical column and increasing left to right along each horizontal row: 5–55 nC per NP by 5 nC per column; dashed line encloses NPs deposited at threshold dose of 15 pC per NP. Inset: *in situ* planar-view of 11 × 11 NP array (200 nm pitch) deposited at 13 nC per NP. (c and e) *Ex situ* tilted views (70°) of the dose array in part (a) at different magnifications. (d and f) *Ex situ* tilted views (70°) of the dose array in part (b) at different magnifications.

facilitate the nucleation and growth of EBID structures, as some studies suggest,[4,13,20,24,25] then the metallic bilayer of the coated Si_xN_4 membrane would prevent the build-up of charge and hence hinder the deposition process. In order to substantiate this hypothesis in the case of LP-EBID, further experiments will be needed.

Purity of Pt deposits

Finally, we present EDS measurements and simulations for representative Pt NPs on bare and coated Si_xN_4 membranes, confirming our previous findings on polyimide membranes[11,14] that e-beam-induced deposits obtained from aqueous precursors of Pt and Au have considerably higher purity than corresponding deposits from metal–organic gas-phase precursors. Parts (a) and (b) of Fig.10 show X-ray spectra for deposits on bare and Au + Cr-coated Si_xN_4 substrates, respectively, including measured spectra of the membranes themselves (*i.e.*, of regions without any LP-EBID structures). The Monte Carlo simulations were performed for *spherical* Pt_yCl_{1-y} particles with the density of *bulk Pt* on *bulk* substrates of *stoichiometric* Si_3N_4, where the italics denote simplifications with respect to the experimental situation of (nearly) hemispherical deposits on thin $Si_{x>3}N_4$ and Au + Cr-coated $Si_{x>3}N_4$ membranes. The simulations were nonetheless useful for estimating the amount of Cl in the experimental deposits, and further trials confirmed that doubling the diameter or halving the density of the Pt_yCl_{1-y} sphere resulted in a relative difference of only about 5% for the Pt(2.33 keV) : Cl(2.62 keV) peak ratio in Fig. 10. Another simplification in the simulated spectra was to neglect e-beam-induced carbon (C) contamination from post-deposition SEM imaging and EDS data acquisition, whereas a C *K–L* peak at 0.28 keV is present in all experimental spectra in Fig. 10, deposits (traces 3 and 6) and substrates alike (traces 1 and 4). Since the H_2PtCl_6(aq) precursor and the Si_xN_4 substrates nominally contain no C compounds, any C impurities must have entered the deposits from *ex situ* sources.

The diameters of the simulated Pt_yCl_{1-y} spheres were chosen such as to yield good correspondence to the ratio of the two largest peaks in each experimental spectrum, Si *K–L* at 1.74 keV and Pt *M–N* at 2.05 keV, namely 370 nm in Fig. 10(a) and 150 nm in Fig. 10(b). Interestingly, these diameters match closely the lateral radii of the experimental NPs used in the EDS measurements (see insets in Fig. 10), and hence the heights of the NPs above the substrate surface if hemispherical shapes are assumed.

Several fractional compositions (Pt : Cl) were simulated to establish upper-bound estimates for the amount of Cl contamination in the deposits by comparing the magnitudes of the Cl *K–L* peak at 2.62 keV in the experimental and simulated spectra. For the Pt_yCl_{1-y} deposits on bare Si_xN_4 (Fig. 10(a)), a simulated spectrum (trace 2) with $y = 0.85$ (85 at% Pt) compares well with the current experimental data (trace 3) as well as with our previous EDS measurements for Pt deposits on polyimide (see ref. 11). In the case of a Au + Cr-coated Si_xN_4 membrane (Fig. 10(b)), a simulation (trace 5) with $y = 0.80$ (80 at% Pt)

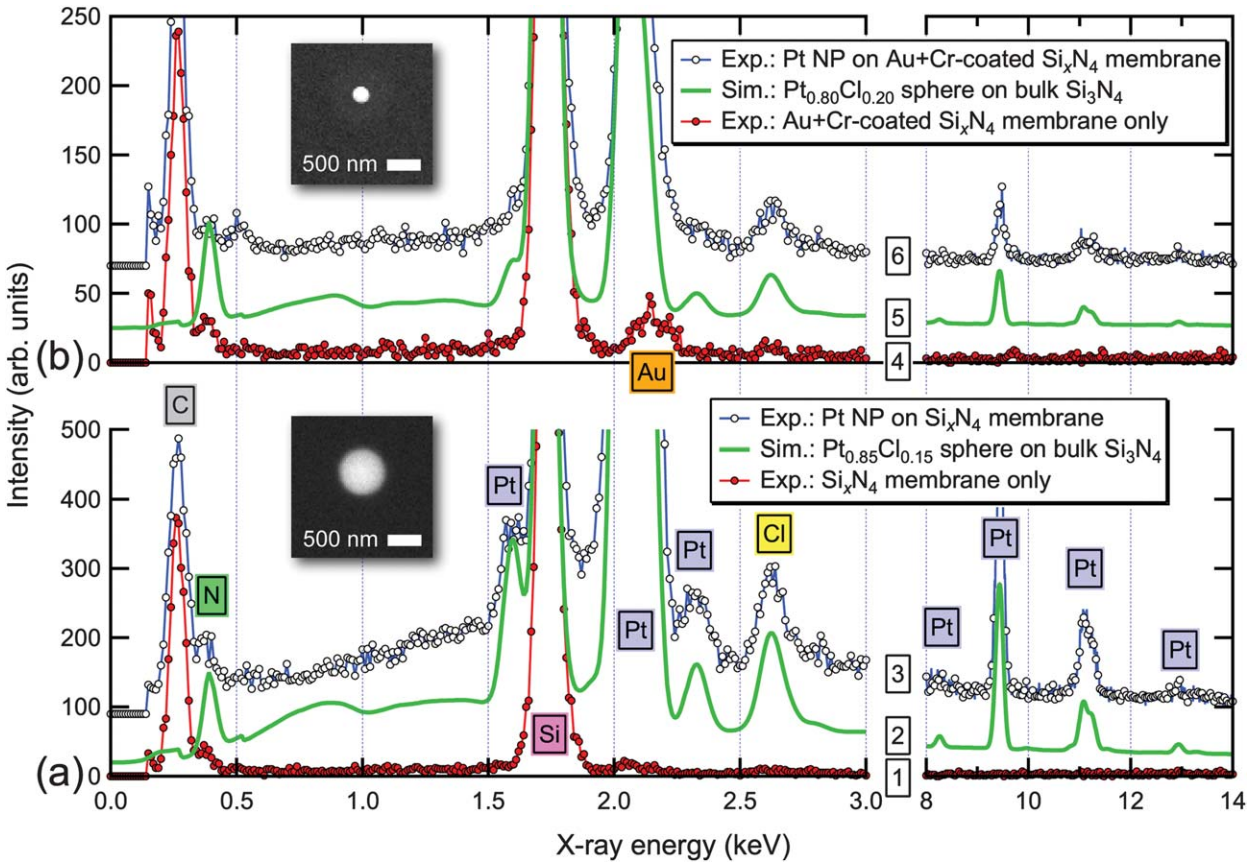

Fig. 10 (Traces 3 and 6) Experimental EDS spectra of single Pt NPs, shown in inset SEM images, on (a) uncoated Si_xN_4 and (b) Au + Cr-coated Si_xN_4 membranes. (Traces 1 and 4) Experimental EDS spectra of the membranes alone, *i.e.*, areas without Pt deposits. (Traces 2 and 5) Simulated X-ray spectra of single Pt_yCl_{1-y} spheres of (a) $y = 0.85$, $2r = 370$ nm and (b) $y = 0.80$, $2r = 150$ nm, both on bulk Si_3N_4 substrates. Traces 2, 3, 5 and 6 are scaled to the corresponding experimental Pt peaks at 2.33 keV and offset vertically for clarity. All axes are truncated for clarity and to exclude an energy region (3–8 keV) with no observable peaks. Characteristic X-ray peaks are labeled with corresponding element symbols. Upper-bound estimates for chlorine (Cl) contamination: 15 at% Cl on bare and 20 at% Cl on Au + Cr-coated Si_xN_4.

provided a good match to the corresponding experimental spectrum (trace 6). By comparison, gas-phase EBID typically yields as-deposited concentrations of 10–15 at% Pt from metal–organic and up to 35 at% Pt from inorganic precursors.[8]

Conclusions

We found that the electron-beam-induced nucleation and growth of platinum nanostructures from aqueous solutions is highly substrate dependent. Depositions on silicon–nitride and gold-coated silicon–nitride membranes differ markedly from deposition on polyimide membranes. Deposition on polyimide membranes is characterized by electron-beam-induced modifications of the membranes that assist in the nucleation and guidance of the growth process at relatively low doses. In contrast, deposition on uncoated Si_xN_4 occurs with little alteration of the membrane and requires orders of magnitude higher dose to initiate deposit growth. Rather than simply promoting deposition and adhesion, coating the Si_xN_4 membranes with a Au + Cr bilayer introduced additional complexity in which a combination of membrane modification and dose-dependent morphologies were observed. This first demonstration of patterned LP-EBID on inorganic substrates highlights the need for greater fundamental understanding of the deposition process. Technologically, the current study brings LP-EBID a step closer to fulfilling its promise of high-purity, high-fidelity nanofabrication with arbitrary materials, substrates, and patterns.

Acknowledgements

This work was partially supported by the Kentucky Science and Engineering Foundation under Grant KSEF-148-502-08-240. This material is also partially based upon work supported by the Defense Advanced Research Projects Agency (DARPA) under Award No. N66001-09-1-2099. Any opinions, findings, and conclusions or recommendations expressed in this publication are those of the authors and do not necessarily reflect the views of DARPA. The authors also thank Brian Wajdyk, Larry Rice, and Stephen Johnson for assistance with the e-beam system, X-ray data acquisition, and e-beam evaporation, respectively. Nicki Davis created Fig. 1.

References

1 R. W. Christy, *J. Appl. Phys.*, 1960, **31**, 1680–1683.
2 A. G. Baker and W. C. Morris, *Rev. Sci. Instrum.*, 1961, **32**, 458–458.

3 S. J. Randolph, J. D. Fowlkes and P. D. Rack, *Crit. Rev. Solid State Mat. Sci.*, 2006, **31**, 55–89.
4 M. H. Song and K. Furuya, *Sci. Technol. Adv. Mater.*, 2008, **9**, 023002.
5 I. Utke, P. Hoffmann and J. Melngailis, *J. Vac. Sci. Technol., B: Microelectron. Nanometer Struct.–Process., Meas., Phenom.*, 2008, **26**, 1197–1276.
6 K. Furuya, *Sci. Technol. Adv. Mater.*, 2008, **9**, 014110.
7 W. F. van Dorp and C. W. Hagen, *J. Appl. Phys.*, 2008, **104**, 081301.
8 A. Botman, J. J. L. Mulders and C. W. Hagen, *Nanotechnology*, 2009, **20**, 372001.
9 N. Silvis-Cividjian and C. W. Hagen, *Electron-Beam-Induced Nanometer-Scale Deposition*, Academic Press, San Diego, 2006.
10 A. Botman, J. J. L. Mulders, R. Weemaes and S. Mentink, *Nanotechnology*, 2006, **17**, 3779–3785.
11 E. U. Donev and J. T. Hastings, *Nano Lett.*, 2009, **9**, 2715–2718.
12 E. U. Donev and J. T. Hastings, *Nanotechnology*, 2009, **20**, 505302.
13 N. Kolmakova and A. Kolmakov, *J. Phys. Chem. C*, 2010, **114**, 17233–17237.
14 G. Schardein, E. U. Donev and J. T. Hastings, *Nanotechnology*, 2011, **22**, 015301.
15 S. Thiberge, O. Zik and E. Moses, *Rev. Sci. Instrum.*, 2004, **75**, 2280–2289.
16 D. R. Ciarlo, *Biomed. Microdevices*, 2002, **4**, 63–68.
17 N. W. M. Ritchie, *DTSA-II*, Deneb edn., 2010.
18 N. W. M. Ritchie, *Microsc. Microanal.*, 2009, **15**, 454–468.
19 N. W. M. Ritchie, *Microsc. Microanal.*, 2010, **16**, 248–258.
20 P. Roy, R. Lynch and P. Schmuki, *Electrochem. Commun.*, 2009, **11**, 1567–1570.
21 M. J. Williamson, R. M. Tromp, P. M. Vereecken, R. Hull and F. M. Ross, *Nature Mater.*, 2003, **2**, 532–536.
22 A. Radisic, P. M. Vereecken, J. B. Hannon, P. C. Searson and F. M. Ross, *Nano Lett.*, 2006, **6**, 238–242.
23 G. Q. Xie, M. H. Song, K. Mitsuishi and K. Furuya, *J. Mater. Sci.*, 2006, **41**, 2567–2571.
24 J. Basu, C. B. Carter, R. Divakar, V. B. Shenoy and N. Ravishankar, *Appl. Phys. Lett.*, 2008, **93**, 133104.
25 C. W. Hagen, W. F. van Dorp and P. A. Crozier, *J. Phys.: Conf. Ser.*, 2008, **126**, 012025.
26 C. W. Hagen, W. F. van Dorp, P. A. Crozier and P. Kruit, *Surf. Sci.*, 2008, **602**, 3212–3219.
27 M. Amman, J. W. Sleight, D. R. Lombardi, R. E. Welser, M. R. Deshpande, M. A. Reed and L. J. Guido, *J. Vac. Sci. Technol., B*, 1996, **14**, 54–62.
28 D. L. Goldfarb, J. J. de Pablo, P. F. Nealey, J. P. Simons, W. M. Moreau and M. Angelopoulos, *J. Vac. Sci. Technol., B*, 2000, **18**, 3313–3317.